Roles of electron mean free path and flux pinning in optimizing the critical current in YBCO superconductors

P. Paturi* and H. Huhtinen

Wihuri Physical Laboratory, Department of Physics and

Astronomy, FIN-20014 University of Turku, Finland

We present a way to reach the maximum possible critical current density, J_c, for YBa$_2$Cu$_3$O$_{6+x}$ (YBCO) thin films. This value is found to be around ten times the currently reached values. It is found that the $J_c(0\text{ T})$ is governed by the mean free path of the electrons, as is the critical temperature, T_c. The J_c in field, on the other hand, is governed by flux pinning sites and can be enhanced by optimizing the size and distribution of the non-superconducting nanoinclusions. By optimizing both the mean free path and the pinning structure, the maximum values can be reached.

I. INTRODUCTION

High-temperature superconductors (HTS), most often YBa$_2$Cu$_3$O$_{6+x}$ (YBCO), have had a lot of promise since their discovery 35 years ago [1] and currently wires are commercially available in kilometre lengths. There are several manufacturing methods for the wires, all with different benefits [2]. Most of the foreseen applications work in magnetic fields of several teslas [2], and there is still a need for improvement in the critical current and critical current density, J_c, of the wires [3]. The highest critical currents are achieved in small samples made with pulsed laser deposition (PLD) as it produces highly crystalline films and supports the growth of rodlike nanoinclusions. The best J_c values in zero and low field and at low temperatures, J_{c0}, are around $6 - 9 \times 10^{11}$ A/m^2 [4]. Although it should be noted that this value is still several times lower than the depairing current and has not essentially increased in the past 20 years [5].

In order to maximize the J_c of the wires, a lot of work has been done in optimizing magnetic flux pinning in the HTS matrix by adding non-superconducting nanoinclusions. The most usual materials, specifically in films made with PLD, are BaMO$_3$ where M is Zr [6, 7], Sn [8], Hf [9] or some other transition metal. The growth morphology of these inclusions depends on the relative mechanical properties of the materials [10, 11] and the growth conditions [12]. Essentially, the

---

*Electronic address: `petriina.paturi@utu.fi`

nanoinclusions act as pinning sites for the magnetic flux quanta, vortices, the movement of which is the cause for the appearance of a voltage at J_c and irreversibility field, B_{irr}.

In addition to the high field properties, the zero and low field critical current density, J_{c0}, should be under investigation as it also limits the J_c in magnetic fields. Despite the vast amount of work done on YBCO, the depairing current has not been reached. It has generally been assumed that it is the maximum value for the J_{c0} [2, 13, 14]. Talantsev *et al* [15, 16] have proposed a different model, which is based on the idea that the low temperature superconductors' Silsbee rule [17] is also valid for high temperature superconductors. According to the Silsbee rule, the superconductor turns into the normal state when the current creates a magnetic field that is higher than the critical field of the superconductor.

In this work, we use a large set of different kinds of YBCO thin films to understand the J_c dependence on the microstructure of the films. All the films have been made at University of Turku, Finland, and the structural and magnetic properties determined immediately after deposition. We find that the electron mean free path is the governing factor in J_{c0}, whereas the high field J_c is determined mostly by the pinning sites. Finally, we propose a way for optimizing the superconductor for different operational conditions and give approximate upper limits for $J_c(B)$.

II.   SAMPLES AND METHODS

All the samples were prepared by pulsed laser deposition (PLD) with a XeCl excimer laser (λ=308 nm) with about 1.5 J/cm^2 laser energy density and 5 Hz repetition frequency. The substrate temperature varied between 725–800 °C in oxygen partial pressure of 175 mTorr. Further details of the PLD system together with deposition parameters have been given elsewhere [18]. The target for the films were prepared in-house as described in [12, 19–25] with either the solid state method or the sol-gel method. All in all, 65 different samples were used.

The samples were chosen so that they represent a large range of YBCO films on different substrates and with artificially produced different pinning sites (APC). Fig. 1 schematically shows the flux pinning site structures in the samples. Typical substrates used for the samples were $SrTiO_3$, Nb-doped $SrTiO_3$, MgO, SLAO, $NdGaO_3$ and LSAT single crystals and buffered, textured and buffered NiW-substrates. In all cases, YBCO grows with c axis perpendicular to the film surface. All the samples were 5×5 mm^2 in size. Thickness of all the films was mostly around 160–220 nm with some single samples of maximum 600 nm and minimum of 100 nm, as measured by transmission electron microscopy (TEM) or atomic force microscopy (AFM).
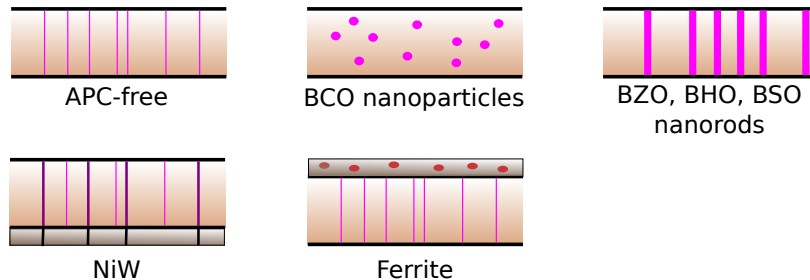
FIG. 1: The main pinning structure in the different samples. See text for details.

In APC-free samples, the main pinning sites in c direction are dislocations; in $BaCeO_3$ (BCO) added samples, BCO forms small 2–4 nm particles whereas in other $BaMO_3$ ($M =$ Zr, Hf, Sn) added samples, the nanorods are formed. In samples on metal substrates (NiW), the substrate grain boundaries transfer to the superconducting layer and thus there are larger low angle grain boundaries in the samples. And finally, the ferrite samples had a CeO_2/ferrite layer($(MFe_2O_4)_{0.4}(CeO_2)_{0.6}$, $M =$ Zn, Co, Ni) on top of the YBCO layer. The pinning structure within the sample is similar to APC-free samples.

The structural properties of the films were measured using Philips X'pert PRO or Philips Empyrean X-ray diffractometers. The analysed XRD data were: 10–110° 2θ scans, detailed rocking curves and 2θ from (005) peaks and 2θ-ϕ scans of the (122)/(212) peak sets. The peaks (004), (005), (007), (0010) and (0011) were used for determination of the c lattice parameter using the Nelson-Riley method and for the determination of the strains using the Williamson-Hall (WH) analysis. The WH size factor was used to estimate the mean free path in the c direction, as explained in the next section. The intensity ratio of the (004) and (005) peaks was also recorded as it indicates the oxygenation level of the sample [26]. The full width at half maximum (FWHM) of the rocking curve of (005) peak was used for the estimation of the mean free path in the ab direction. The instrumental width of 0.02° was subtracted from the widths. In cases where the peaks of (122)/(212) were clearly separate, they were used for calculating the a- and b-lattice parameters and determination of the ϕ width.

The critical current densities, J_c, were defined from magnetization data using the Bean critical state model [27]

$$J_c = \frac{3\Delta M}{a^3 d}, \tag{1}$$

where ΔM is the opening of the magnetic hysteresis loop, a is the lateral size of the square sample (5 mm) and d is the film thickness. The measurements were done using Quantum Design PPMS

with the ACMS-option at 10 K and the hysteresis loops were measured in fields -8 T – 8 T. The low temperature zero field J_c was defined from the zero field values obtained this way. With all measurement methods, the $J_c(B)$ is observed to have a plateau below some accommodation field B^*. In this region the J_c has a constant value, which we will denote as the zero-field J_c, J_{c0}, from now on. It should be noted that in the magnetic measurement the internal magnetic field is not truly zero. Determining J_c from magnetic measurements with the Bean model is well-known to underestimate the J_c at low fields, especially if the area of the film is very small and it is thick ($a/d < 10$) and the starting field of the measurement is too low to fully close the loop [28, 29]. In our case, the aspect ratio of the films was $a/d \approx 2500$ and the starting field was always 8 T, which minimises the discrepancy in low fields. Also, it has been noted that the magnetically measured J_c values are consistently lower than those from transport measurements [30], but in this case all J_cs were determined with the same method.

The critical temperature, T_c, was determined from the peak position in the imaginary part of AC susceptibility temperature dependence data. This corresponds well with the middle of the transition in the real part of the AC susceptibility curve. The width of the superconducting transition was taken to be the full width at half maximum (FWHM) of the AC susceptibility peak. Using the imaginary peak instead of the real part onset or middle temperature makes the determination of T_c less prone to suffer from experimental noise and is more suitable for automated analysis such as used here. This accounts for the somewhat lower T_c values than the usually reported magnetically measured onset or the resistively measured T_c values.

III.   ELECTRON MEAN FREE PATH FROM THE XRD COHERENT DOMAIN SIZE

The main physical parameters defining the superconductor, the coherence length ξ and the magnetic penetration depth λ depend on the electron mean free path in the normal state, as shown by Pippard [31]. All defects that disturb the periodicity of the lattice will decrease the mean free path and increase the normal state resistivity. At the same time, the same defects will also widen the XRD peaks and decrease the coherent domain size of x-rays. Therefore, the XRD coherent domain size and the electron mean free path describe the same phenomenon, as also seen in other materials, e.g. [32, 33]. The nature of the defect does not affect the analysis.

One gets the coherent domain size in the c direction using the Williamson-Hall (WH) analysis of the $(00l)$ peaks. The WH size factor, ϵ, is inversely proportional to the domain size

$$D_c = \frac{K}{\epsilon}, \tag{2}$$

where K is a proportionality constant, usually taken to be 0.92 [34].

An estimate of the coherent domain size in the ab direction is obtained from the width of the rocking curve of the (005) peak using the Scherrer formula [35]

$$D_{ab} = \frac{K}{\beta_x(S)} = \frac{K\lambda}{\beta_\omega 2\sin\theta}, \tag{3}$$

where β_ω is the full width at half maximum (FWHM) of the rocking curve, K is a proportionality constant, 0.92, λ is the x-ray wavelength and θ is the peak position.

The electron mean free path, ℓ, can be determined from the resistivity, ρ, and carrier density, n, obtained from Hall-data, as

$$\ell = \frac{mv_F}{e^2 n}\frac{1}{\rho}, \tag{4}$$

where $v_F = 250$ km/s is the Fermi-velocity for YBCO [36], e is the electron charge and m is the electron mass. The normal state resistivity at 100 K of a set of BCO-added and APC-free samples used in this work has been measured earlier [21]. As the peak widths come from YBCO peaks, the actual nature of the defect does not matter in this analysis. The carrier density in YBCO thin films does not appreciably change by adding APCs [37] and can be taken to be 5×10^{27} m^{-3}. Figure 2 shows the calculated mean free path for the BCO-added YBCO samples as functions of the XRD size parameters obtained from the (005) rocking curve, D_{ab}, and WH analysis of (00l) peaks, D_c. The data fall surprisingly well to lines with the same slope. The difference in the zero-point value between the c and ab directions is 4 Å, i.e. quite small.

In the following, we use the mean free paths determined from this analysis for each sample.

IV.   ZERO FIELD J_c, T_c AND THE MEAN FREE PATH

Plots of J_{c0} and T_c as functions of all the determined parameters are shown in the supplementary information (SI). Here we concentrate on results which explain the J_{c0} and T_c values and the shape of the $J_c(B)$ curve.

To investigate the effect of the electron mean free path on J_{c0}, we have plotted the measured J_{c0} as the function of ℓ in Fig. 3(a). There is a clear correlation between ℓ and J_{c0}, where the J_{c0} increases with increasing ℓ. Pippard [31] has presented a well-established, mostly phenomenological, model for taking into account the effect of defects. According to the model, the lowered electron mean free path, ℓ, in the superconductor shortens the coherence length as

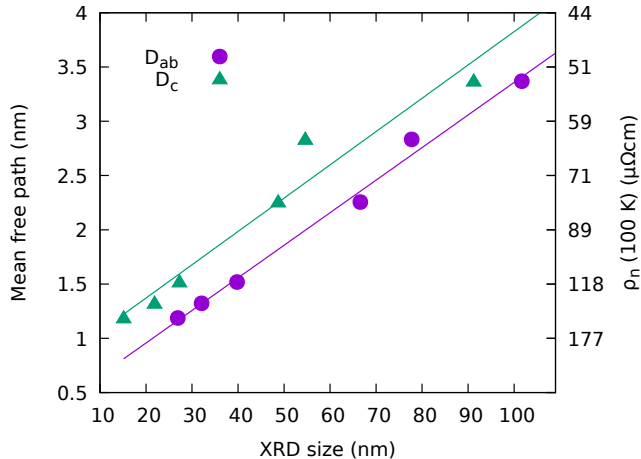$$\frac{1}{\xi} = \frac{1}{\xi_0} + \frac{1}{\ell}, \tag{5}$$

FIG. 2: The mean free paths determined from the resistivity data [21] with Eq. (4) as the function of the XRD size parameters, D_{ab} and D_c. The lines are linear fits to the data. The right hand scale shows the measured normal state resistivities.

where ξ_0 is the clean limit coherence length and ℓ is the electron mean free path. Similarly for penetration depth

$$\lambda = \lambda_0 \sqrt{1 + \xi_0/\ell}, \tag{6}$$

where λ_0 is the clean limit penetration depth.

Quite often it is assumed that the depairing current [38]

$$J_{\mathrm{c,depair}} = \phi_0/4\pi\mu_0\lambda^2\xi, \tag{7}$$

is the defining factor that determines J_{c0}. Inserting the above ℓ dependence, one easily finds that $J_{\mathrm{c,depair}}$ is independent of ℓ. This is shown as the red horizontal line in Fig. 3(a). To get the correct value for J_{c0}, one needs to assume $\lambda_{ab} = 770$ nm, which is several times of any of the experimental values. Clearly, the observed J_{c0} of YBCO cannot be explained by the depairing current.

For type I superconductors, the situation, where the magnetic field induced by the current in the superconductor exceeds the critical field and causes the return to normal state, has been known as the Silsbee rule for over 100 years [17]. Talantsev et al [15] have suggested that for HTS, the Silsbee limiting magnetic field is the lower critical field H_{c1}. The idea is that when the current is at the critical value, the magnetic field along the flat surface caused by the current is high enough for the vortices to enter the superconductor causing dissipation and return it to the normal state. It should be noted that the critical current flowing in the sample in the remanent state produces

a similar magnetic field around the edge of the superconducting film as the transport current in a transport measurement [39] and therefore the Talantsev model can be used also for J_{c0} obtained from magnetization data. Using H_{c1} as the critical field, we get $J_{c0} = H_{c1}/\lambda$, where H_{c1} depends on λ and the coherence length, ξ, as [15]

$$H_{c1} = \frac{\phi_0}{4\pi\mu_0\lambda^2}(\ln\kappa + 0.5), \tag{8}$$

where $\kappa = \lambda/\xi$. In anisotropic YBCO thin films, the J_{c0} is further modified into [15]

$$J_{c,0} = \frac{H_{c1}}{\lambda_{ab}} \times \frac{\lambda_c}{d}\tanh\frac{d}{\lambda_c}, \tag{9}$$

where λ_i are the penetration depths in the ab and c directions and d is the thickness of the film. The obtained J_{c0} values are of the same order of magnitude as the measured values.

The J_{c0} data can easily be fitted with Eq. (9) (shown as the purple curve in Fig. 3(a)) using $\lambda_{0,ab}$ as the only fitting parameter. The obtained value is 87 nm, when anisotropy parameter $\gamma = 5$ is assumed [13]. This value of λ is within the experimental values [40][52], although at the low end. These values are obtained in very pure detwinned single crystals and since λ_0 is the value the model approaches, it is what should be expected. Typical thin films contain a large amount of defects which decrease ξ and increase λ to the more typically observed $130 - 150$ nm.

The third commonly claimed option for the main determining factor of J_{c0} is pinning. In low magnetic fields, the vortex-vortex interaction is negligible, and we can concentrate on the pinning force caused by the strongest pinning sites in the superconductor. In $B||c$ direction, the strongest pinning sites are columnar non-superconducting inclusions, such as $BaZrO_3$ or $BaSnO_3$ nanorods. For this type of pinning site, the critical current density is [13]

$$J_{c,pin} = \begin{cases} \frac{27\sqrt{2}}{64}\left(\frac{r_r}{2\xi}\right)^2 J_{c,depair} & r_r < \sqrt{2}\xi, \\ \frac{3\sqrt{3}}{4\sqrt{2}}J_{c,depair} & \sqrt{2}\xi < r_r < \lambda, \end{cases} \tag{10}$$

where r_r is the radius of the pinning site and ξ is the coherence length (the discontinuity is in [13], but does not affect our conclusion). Assuming an average pinning site radius of 0.5 nm and the change in the coherence length due to the decrease of the electron mean free path, we get the blue line shown in Fig. 3(a). Here, the fitted $\lambda_{ab} \approx 883$ nm is also clearly out of the experimental range. The dependence on ℓ is opposite to what is observed, so pinning does not explain J_{c0}. For larger pinning sites, the $J_{c,pin}$ is similar to $J_{c,depair}$ at all ℓ.

In addition, it can be seen that the structure, size and density of flux-pinning sites are not the determining factors of J_{c0} from observing the values of different kinds of samples. The largest
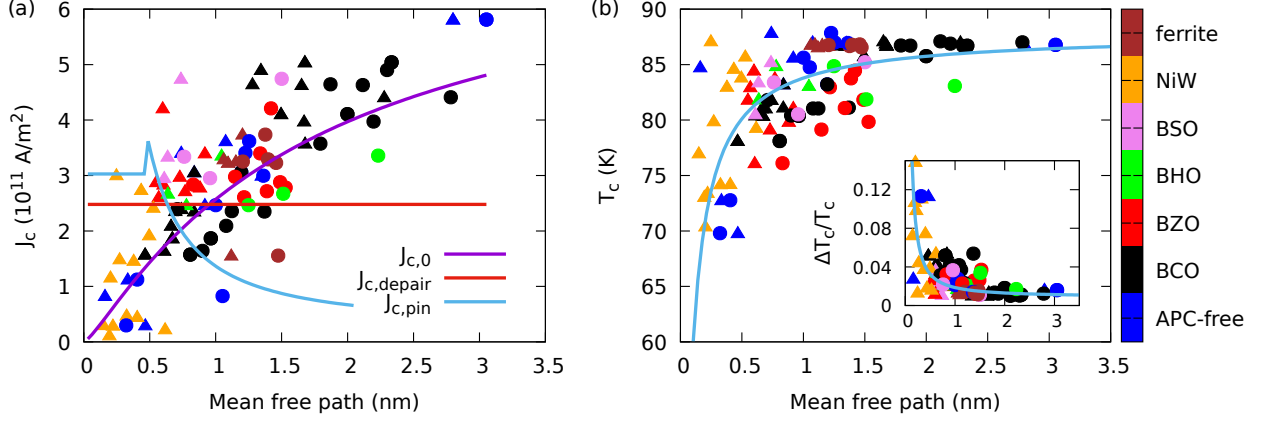
FIG. 3: (a) J_{c0} of the samples as the function of the estimated mean free path. The different colours of the symbols represent different types of samples and the triangles are the ℓ from the WH analysis and the circles from the rocking curve of (005) peak. The purple upward curve is a fit for Eq. (9), the red horizontal line a fit for the depairing current Eq. (7) and the blue decreasing curve a fit to the pinning J_{c0}, Eq. (10) (The discontinuity is shown as in the original source [13]). (b) T_c as function of the mean free path similarly as in (a). The line is a fit for Eq. (11). The inset shows the relative transition width as the function of the mean free path similarly as the main panel. The line is a fit for Eq. (12)

pinning sites (about 10 nm in diameter) in our set are in the $BaSnO_3$ added samples, $BaZrO_3$ nanorods are around 5 nm in diameter and $BaCeO_3$ particles are around 3 nm. According to Eq. (10), J_{c0} should be clearly the highest for the $BaSnO_3$ added samples, then $BaZrO_3$ samples and last $BaCeO_3$ and APC-free samples. Clearly, this kind of dependence is not observed; instead the highest J_{c0} is observed in APC-free and $BaCeO_3$ added samples.

In the traditional view, the critical temperature, T_c, should not be affected by non-magnetic impurities [41, 42], but they do lower the T_c in HTS [43, 44]. It has been modelled with the Abrikosov-Gor'kov theory, which can be written as [43]

$$T_c = \frac{T_{c0}}{1 + \alpha 0.882\frac{\xi_0}{\ell}},\qquad(11)$$

where α is a numeric parameter proportional to the pair-breaking effectiveness of scattering by impurities. The main panel of Fig. 3(b) shows the measured T_c values as the function of ℓ and the fit to Eq. (11). The obtained fitting parameter is $\alpha = 0.042$, which is of the same order of magnitude as observed earlier [43]. It is clear from Fig. 3(b) that the maximum value of T_c in the data is close to 87 K instead of the generally agreed 92 K for YBCO. This is due to the method of determining T_c from the maximum of the imaginary AC-magnetization curve, which is always lower than the resistive transition. The highest onset temperatures are around 92 K.

The transition width is generally thought to be a measure of the goodness or purity of the sample [38]. The inset of Fig. 3(b) shows the transition width, ΔT_c, divided by T_c. B. B. Goodman [45] has proposed that the width of the transition depends on the coherence length as

$$\frac{\Delta T_c}{T_c} = 1.11 \left(\frac{k_B}{\pi c_n \xi^3} \right)^{1/2},$$ (12)

where c_n is the normal state specific heat and k_B is the Boltzmann constant. Using the impurity limited coherence length $\xi(\ell)$ (Eq. (5)), we get the line shown in the inset of Fig. 3(b). Although there is quite a lot of scatter, the model holds quite nicely. The reason for the increase of the width of the transition is fluctuations of energy in small volumes, the size of which is determined by the coherence length. Upon decreasing temperature, some of those volumes become superconducting and the rest stay normal. Smaller domains, due to the restriction of the coherence length by the mean free path, lead to greater number of these volumes and thus larger transition width.

V. HIGH FIELD PROPERTIES

Let us next turn our attention to the high field properties of the films. In high fields, the essential property for applications is the $J_c(B)$ dependence.

A typical method of describing the field dependence of J_c is to fit $J_c \propto B^{-\alpha}$ above the field where $J_c = 0.9 J_{c0}$ [46]. Since the samples with strong pinning sites do not follow this dependence well enough [47], analysis based on the pinning force, F_p was done. In the measurement conditions here, $F_p = J_c B$ (since $B \perp J_c$) and the fitting was done to the Dew-Hughes equation [48]. Prior to fitting, $F_p(B)$ was scaled with the maximum values of F_p and B as in [47]. In this case, we get

$$\begin{aligned} F_p(B) &= F_{p0} \left(\frac{B}{B_{\text{irr}}} \right)^p \left(1 - \frac{B}{B_{\text{irr}}} \right)^q \\ &= F_{p,max} \frac{(p+q)^{p+q}}{p^p q^q} \left(\frac{B}{B_{\text{max}}} \frac{p}{p+q} \right)^p \left(1 - \frac{B}{B_{\text{max}}} \frac{p}{p+q} \right)^q. \end{aligned}$$ (13)

B_{max}, F_{max} and p were fitted and $q = 1.1$ was used for all samples, since at low temperature, the effect of the last term in Eq. (13) is negligible.

Theoretically, the obtained p values should be in the range $0.5 - 1$, where $p = 0.5$ is typically obtained from APC-free films with dislocations, stacking faults and twins as the main pinning sites, that is when the pinning sites are small compared to ξ. In films, which contain non-superconducting nanorods (e.g. BZO, BSO, BHO), p increases up to 1 depending on the diameter of the rod, i.e. the pinning strength of the rod as in Eq. (10) [47]. Value of $p = 1$ implies that J_c does not

decrease with the magnetic field at all below very high fields, where the q-part of Eq. (13), due to vortex-vortex interaction, starts to bend the F_p curve downwards.

In Fig. 4(a) are shown the p values for all the films as the function of the mean free path. The samples known to have nanorods are marked with open symbols, otherwise the symbols are the same as before. It is clearly seen that there is a clear difference between the different types of films and that the mean free path is not the main factor determining p. The samples with large nanorods (in the yellow ellipse) have very high p values, which indicates that the pinning sites are strong enough to break the vortex lattice and individually pin the vortices.

In the other samples, p decreases, roughly linearly, with increasing mean free path. In these samples, the main pinning sites are dislocations, twins, stacking faults and other small crystallographic defects, which are not strong enough to break the vortex lattice on their own, which would lead to $p \approx 0.5$ [49]. The observed increase of p with the decreasing mean free path can be understood to be caused by the increasing number of pinning sites, in addition to the increase in the effective size of the pinning sites. The effective size of a pinning site can increase e.g. when the strain field around a defect is enlarged and the superconducting order parameter is depressed. This kind of crystal lattice distortion also leads to the decrease of the mean free path. It has been observed [50] that p depends continuously on the size of the pinning sites, and this is due to the gradual breaking of the vortex lattice when the pinning force overcomes the vortex lattice elastic forces.

It should be noted that in contrast to J_{c0} and T_c, where the mean free path was found to be the direct cause of the change of value, here the crystal defects affect both the pinning and the mean free path, sometimes in opposite directions. As seen from Fig. 3(a), the J_{c0} dependence caused by pinning is opposite to what is observed.

Similarly to p, the determined pinning forces are shown in Fig. 4(b). Here, no dependence on the mean free path is seen. The samples without nanorods fall on a wide horizontal zone shown by the yellow thick line, whereas the nanorod containing samples have clearly larger pinning forces. According to the pinning models, the maximum pinning force is proportional to the energy increase needed to remove the vortex from the pinning site. It is obtained that [14]

$$F_{p0}(\ell) \propto \xi(\ell)\mu_0 H_c(\ell)^2, \tag{14}$$

where $H_c(\ell) = \phi_0/(2\sqrt{2}\lambda(\ell)\xi(\ell))$ and the proportionality constant depends on the size of the pinning site. Thus, the pinning force is independent of ℓ. The samples with small pinning sites are shown as filled symbols in Fig. 4(b) and all these fall onto the same level. Clearly, a different
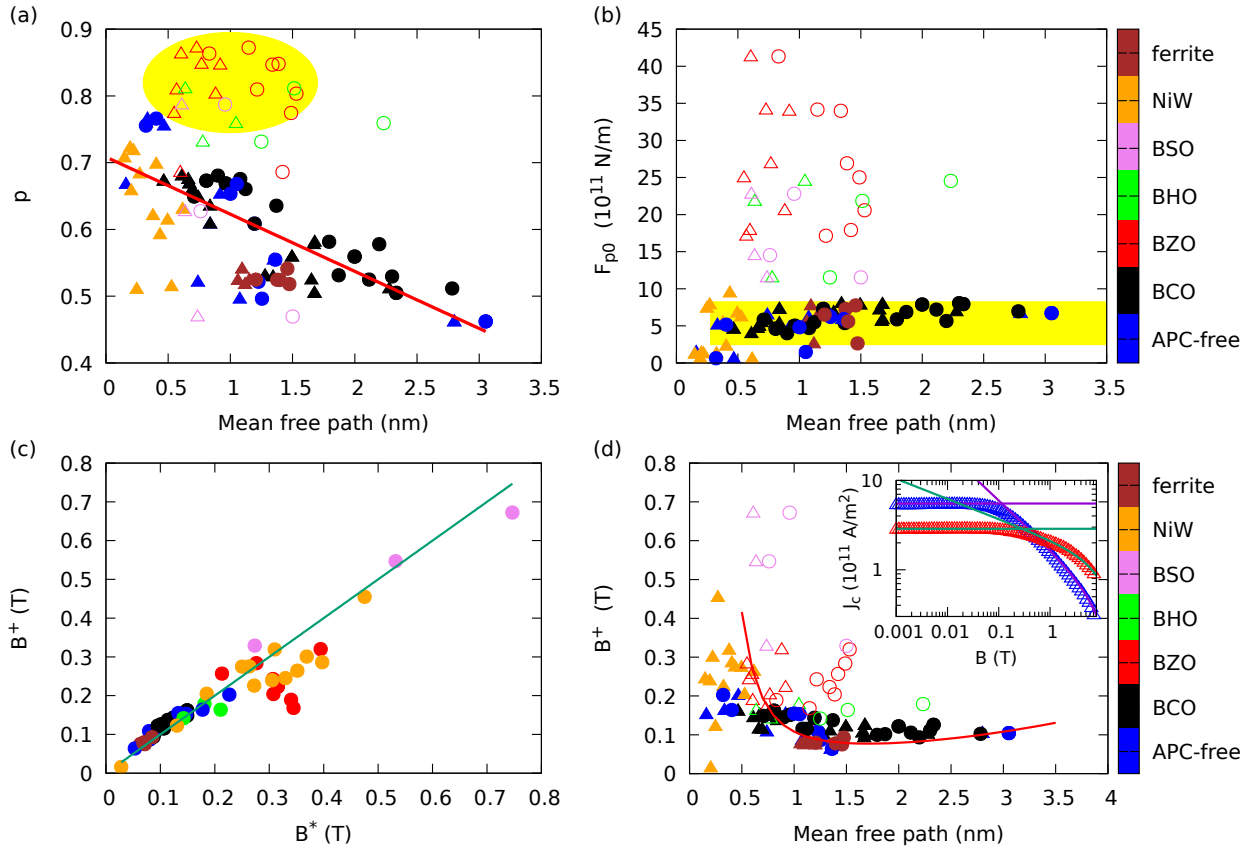
FIG. 4: (a)The fitted p values as determined from fits to Eq. (13). The open symbols are samples that are known to have non-superconducting nanorods, the colours, triangles and circles are the same as in previous figures. The red thick line highlights the approximate correlation in samples with just dislocations, twins and non-correlated BCO particles. (b) The calculated F_{p0} values calculated from the fitted $F_{p,max}$ values as determined from fits to Eq. (13) similarly as in (a). The yellow thick line highlights the approximate correlation in samples with just dislocations, twins and non-correlated BCO particles. (c) The determined B^+ as function of B^* values. The slope of the line is 1. (d) The determined B^+ values similarly as in (a). The solid red line shows the calculated crossing of Eqs. (13) and (9) with $B_{max} = 5$ T, $q = 1.1$, $F_p = 5 \cdot 10^{11}$ N/m and $p = -0.087\ell + 0.68$ (with ℓ in nm) obtained from (a). The inset shows $J_c(B)$ curves for an APC-free (blue) and BZO-added films (red) together with the fits to Eq. (9) and Eq. (13). B^+ is defined as the crossing of these curves. Note, that no fitting is done.

mechanism is working for the samples with nanorods. In these samples, the vortices can fit into the pinning site and the pinning force of an individual pinning site is determined by the size of the pinning site [13]. It should be again noted that the maximum pinning force is not defined directly by the electron mean free path, but rather by the size of the pinning sites.

At low magnetic fields, the J_c is determined by the mean free path (Eq. (9)), whereas at

large fields it is defined by the structure, size and density of pinning sites. The mechanism which produces lower J_c values determines the experimental value. The crossover from one mechanism to the other happens at the crossover field, B^+. B^+ is essentially the same as the generally used accommodation field B^*, which is usually defined from the field value where $J_c = 0.9\ J_{c0}$. Defining it from the crossing of the fits is less ambiguous and accounts for the entire $J_c(B)$ curve without a need to determine the ranges of the fitting by hand. Fig. 4(c) shows the determined B^+ as a function of the B^* values. It is clearly seen that B^+ and B^* are identical in the samples with small pinning sites, but there is more deviation in the values for samples with large pinning sites. The difference between these samples is that with large pinning sites the p exponent is close to 1 and the $J_c(B)$ curve is very rounded. This makes the definition of B^* subject to errors. This emphasizes the need for the new method of defining the field where the main cause of J_c changes. The inset of Fig. 4(d) shows the ease of determining B^+ for an APC-free and a BZO-added sample.

Fig. 4(d) shows the crossover fields, B^+, numerically solved from crossing of the fits to the pinning force (Eq. (13)) and the zero field J_c (Eq. (9)) for each sample. Clearly, the samples with nanorods (open symbols, the main panel of Fig. 4(d)) form again a group of their own. Especially those with large BSO nanorods have higher B^+. These are the samples with p close to 1 and hardly any field dependence of J_c at low temperatures, which increases the B^+ values. For most of the samples, B^+ decreases with increasing electron mean free path. Qualitatively, this is easily understood by the fact that increasing the number of lattice defects decreases the mean free path, while at the same time they act as pinning sites for the vortices. Similar dependence of B^* on number of dislocations was observed already in [46]. For a more quantitative analysis, the crossing of Eq. (13) and Eq. (9) was numerically solved using the values obtained earlier in this analysis and the mean free path dependent p and $B_{irr} = (p+q)B_{max}/q$. The used values are given in the caption of Fig. 4(d). It should be noted that no fitting was done. The model describes the overall trend in the data well.

VI.   REACHING MAXIMUM J_c IN $B||c$ DIRECTION

Based on the results in this work, we can make the following conclusions:

1. The zero and low field J_c is determined by the coherence length and penetration depth of the superconductor. These are strongly dependent on the electron mean free path in the superconductor.

2. The critical temperature and the width of the transition are also determined by the mean free path.

3. The critical current at high fields is mainly determined by the flux pinning sites of the sample and can therefore be increased by adding non-superconducting APCs.

4. With increasing magnetic field, the transition from mostly mean free path limited J_{c0} to pinning limited J_c takes place at the crossover field B^+. When $B > B^+$, $J_{c,\text{pin}} < J_{c0}$.

The obvious problem is that increasing J_{c0} requires increasing the electron mean free path, but adding APCs decreases it. In most power applications, the aim is to have as high J_c as possible at magnetic fields around $3 - 5$ T [2, 51]. In order to design the best possible pinning landscape, let us analyse the $J_c(B) = F_p(B)/B$ curve (Eq. (13)) in more detail.

We start by assuming that the effect of exponent q is very small and can be taken to be 1, since its effect was also found negligible in the experimental analysis. To achieve high $J_c(B)$ values at high fields, one needs to increase the exponent p up to 1. This can be done by increasing the nanorod diameter above 5 nm (e.g. by using BSO as APCs). In the case where $p = 1$, the flux lattice is broken and the total pinning force can be summed as $F_{p,max} = N f_p$, where N is the number of pinning sites and f_p is the pinning force of the individual pinning site [14].

In order to estimate the size of the optimal pinning site, we can use the model for strong pinning sites [13], which gives us the pinning potential as function of distance. To get the maximum pinning force one must differentiate the potential and take the maximum value at $r = r_r$. Doing so, we get

$$f_{p,max}(r_r) = \frac{\epsilon_0 r_r^2}{\xi} \left(\sqrt{2} r_r + \xi \right)^{-1} \left(r_r + \sqrt{2} \xi \right)^{-1}, \tag{15}$$

where $\epsilon_0 = \phi_0^2/\mu_0(4\pi\lambda)^2$ is the energy scale of vortices and r_r is the radius of the pinning site. $f_{p,max}$ increases with increasing r_r, but quite slowly when $r_r \gtrsim 4$ nm. The number of pinning sites N is proportional to the inverse square of the distance between them and thus

$$F_{p,max} \propto f_{p,max}(r_r)/d_r^2, \tag{16}$$

where d_r is the average distance between the nanorods (centre-to-centre). F_{p0} is obtained from $F_{p,max}$ as in Eq. (13). F_{p0} increases with increasing nanorod size and density. Naturally, there have to be some physical limits to these, the absolute minimum for d_r is when there is no superconductor left between the rods. Also, the summation rule assumption is only valid for $r_r \gtrsim 2$ nm.

After optimizing F_{p0}, let us turn to the irreversibility field, B_{irr}. B_{irr} is defined as the field, where the measured critical current is zero. Following the calculation in [14] and taking the volume
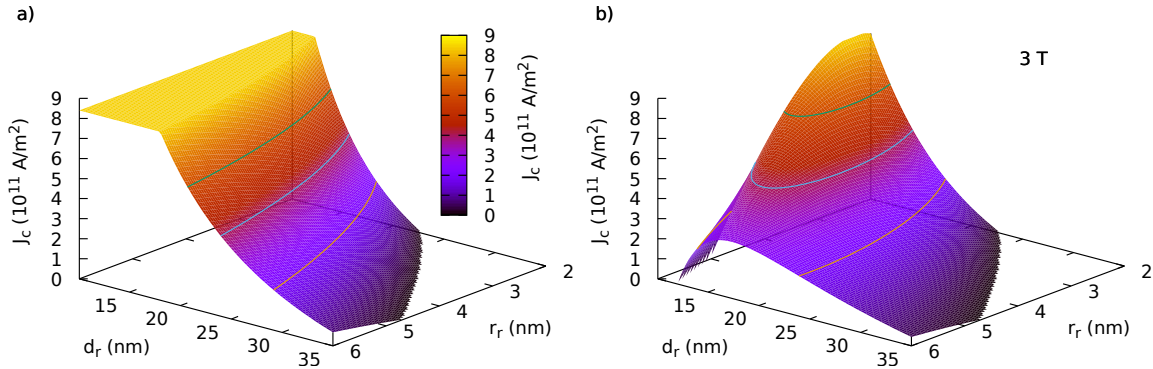
FIG. 5: a) The calculated optimized J_c as function of rod radius, r_r and distance d_r at 3 T field using the optimized values $J_{c0} = 8.4 \times 10^{11}$ A/m² and $\lambda = 87$ nm. b) The same dependence, but taking into account the decreasing superconducting cross-section with increasing amount of APCs. The constant J_c contours are meant to ease seeing the shape of the surface.

fraction of the pinning sites to be $f = \pi r_r^2/d_r^2$, we get

$$B_{irr} = 16.84d \left(\frac{r_r \phi_0 T^4 \zeta^4 J_{c,0} \log(B_{irr} a_0 \nu_0/E_c)}{d_r^2 \xi} \right)^{1/3} \approx 235.8 \; d \left(\frac{r_r \phi_0 T^4 \zeta^4 J_{c,0}}{d_r^2 \xi} \right)^{1/3}, \qquad (17)$$

where d is the thickness of the film, T is the temperature and ζ is a constant of around 4–6, which scales the interaction distance of the vortices and depends on the type of the pinning sites. The logarithmic term depends on the attempt frequency (ν_0) and the depth of the potential well (E_c). Fortunately, due to the logarithmic nature, it can be taken to be about 14 in all reasonable cases [14], which enables obtaining an analytic expression for the B_{irr}.

Combining the above analysis to $J_c = F_p/B$, we get the dependence shown in Fig. 5(a) for magnetic field of 3 T. The result is intuitively correct as J_c increases with increasing rod size and decreasing rod distance. The plateau at small d_r is the area where J_c is determined by J_{c0}. We still need to take into account that adding nanorods decreases the superconducting cross-section by the factor of $1 - 2r_r/d_r$. Multiplying that to the J_c, we get the dependence shown in Fig. 5(b). It is clearly seen that there is an optimal size and density for the nanorods. These optimal values depend on the used magnetic field as shown in Fig. 6(a) where one can read the optimal distance between the rods from the color scale by choosing the magnetic field and rod size. The result is intuitively correct as increasing r_r and decreasing field lead to larger distance between the rods and thus higher J_c.

We can now describe the best possible YBCO superconductor for applications. At low magnetic
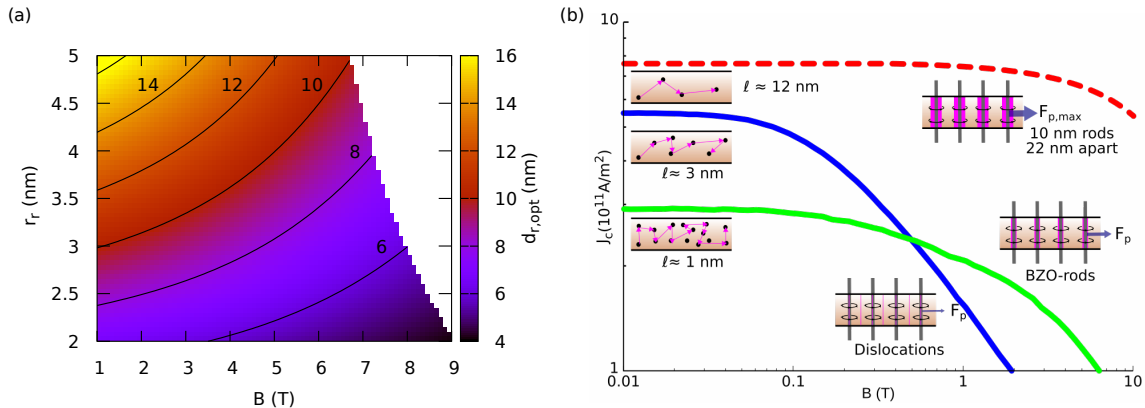
FIG. 6: (a) The optimal distance between nanorods of radius r_r at different magnetic fields. In the empty upper right corner the rods would fill the whole sample. (b) In order to maximize J_c in the whole field range, one needs to increase the mean free path, ℓ, and add large nanorods to obtain $p = 1$. The blue and green lines are measured data for APC-free and BZO-added samples, respectively. The mean free path of the APC-free sample is about 3 nm, but the main pinning sites lead to small pinning force. BZO-nanorods decrease ℓ to 1 nm, but increase the F_p considerably. The optimal sample would have large $\sim$10 nm nanorods about 22 nm apart (centre-to-centre) and very long ℓ, as shown by the red dashed curve.

fields, the limiting factor of J_{c0} is the mean free path of the electrons and increasing that to the clean limit gives maximum $J_{c0} \approx 8.4 \times 10^{11}$ A/m^2. Note, that this is very close to the reported maximum values [4]. At high fields, J_c is limited by the structure, size and density of pinning sites. and the maximum is obtained with high density large nanorods. Fig. 6(b) shows the $J_c(B)$ curves for an APC-free YBCO sample and one with BZO-nanorods as well as an imaginary sample with high mean free path and 10 nm diameter nanorods with distance (centre-to-centre) of 22 nm. The most critical parameter to increase is the mean free path as the level of the $J_c(B)$ curve also depends on J_{c0}. The practical problem is to ensure as defect-free YBCO between the rods as possible. In PLD, this is a question of optimizing the deposition parameters carefully. Undoubtedly, reaching $\ell > 6$ nm is very difficult, but even by increasing ℓ up to the level of APC-free YBCO in samples with rods would increase the J_c in the application field range by about factor of 10.

VII. CONCLUSIONS

We have analysed the structural and superconducting properties of a large set of YBa$_2$Cu$_3$O$_{6+x}$ (YBCO) thin films with different kinds of artificial pinning sites. It was found that the J_c at zero

field is determined by the electron mean free path, as is the critical temperature, T_c. The J_c in field, on the other hand, is governed by flux pinning sites and can be enhanced by optimizing the size and distribution of the non-superconducting nanoinclusions. It should be remembered, though, that the J_c0 also limits the $J_\mathrm{c}(B)$.

By optimizing both, the mean free path and the pinning structure, the maximum value of $J_\mathrm{c}(B)$ can be reached. This value was found to be around ten times the currently reached values. On the other hand, it seems that the maximum J_c0 has been reached with the crystallographically best samples already 20 years ago.

In practice, this means that the superconductor in between the pinning sites should be as crystallographically clean as possible to increase the electron mean free path. The optimal pinning site size and density depend on the planned magnetic field. For a field of 5 T, the pinning site diameter should be around 10 nm and the distance 20 nm, i.e. the density should be quite high.

---

[1] J. G. Bednorz and K. A. Müller, Z. Phys. B **64**, 189 (1986).

[2] X. Obradors and T. Puig, Supercond. Sci. Technol. **27**, 044003:1 (2014).

[3] A. C. Wulff, A. B. Abrahamsen, and A. Insinga, Supercond. Sci. Technol. **34**, 053003 (2021).

[4] A. Stangl, A. Palau, G. Deutscher, X. Obradors, and T. Puig, Scientific reports **11**, 8176 (2021).

[5] H. Huhtinen, P. Paturi, E. Lähderanta, and R. Laiho, Supercond. Sci. Technol. **12**, 81 (1999).

[6] J. L. MacManus-Driscoll, S. R. Foltyn, Q. X. Jia, H. Wang, A. Serquis, L. Civale, B. Maiorov, M. E. Hawley, M. P. Maley, and D. E. Peterson, Nat. Mater. **3**, 439 (2004).

[7] M. Peurla, H. Huhtinen, P. Paturi, Y. P. Stepanov, J. Raittila, and R. Laiho, IEEE T. Appl. Supercond. **15**, 3050 (2005).

[8] C. V. Varanasi, P. N. Barnes, J. Burke, L. Brunke, I. Maartense, T. J. Haugan, E. A. Stinzianni, K. A. Dunn, and P. Haldar, Supercond. Sci. Technol. **19**, L37 (2006).

[9] H. Tobita, K. Notoh, K. Higashikawa, M. Inoue, T. Kiss, T. Kato, T. Hirayama, M. Yoshizumi, T. Izumi, and Y. Shiohara, Supercond. Sci. Technol. **25**, 062002 (2012).

[10] J. J. Shi and J. Z. Wu, Philosophical Magazine **92**, 2911 (2012).

[11] J. J. Shi and J. Z. Wu, J. Appl. Phys. **118**, 164301:1 (2015).

[12] M. Malmivirta, L. Yao, H. Huhtinen, H. Palonen, S. van Dijken, and P. Paturi, Thin Solid Films **562**, 554 (2014).

[13] G. Blatter, M. V. Feigel'man, V. B. Geshkenbein, A. I. Larkin, and V. M. Vinokur, Reviews of Modern Physics **66**, 1125 (1994).

[14] T. Matsushita, *Flux pinning in superconductors*, 1895 (Springer, Heidelberg, Germany, 2007).

[15] E. F. Talantsev and J. L. Tallon, Nature Communications **6**, 7820 (2015).

[16] E. F. Talantsev, W. P. Crump, and J. L. Tallon, Scientific reports **7**, 10010 (2017).

[17] F. B. Silsbee, Journal of the Washington Academy of Sciences **6**, 597 (1916).

[18] H. Palonen, H. Huhtinen, M. A. Shakhov, and P. Paturi, Supercond. Sci. Technol. **26**, 045003:1 (2013).

[19] M. Malmivirta, H. Huhtinen, Y. Zhao, J.-C. Grivel, and P. Paturi, J. Low Temp. Phys. **186**, 74 (2017).

[20] M. Malmivirta, J. Jyrinki, H. Huhtinen, A. V. Pan, S. Rubanov, R. Jha, V. P. S. Awana, and P. Paturi, IEEE T. Appl. Supercond. **27**, 8000705 (2017).

[21] M. Malmivirta, H. Palonen, S. Inkinen, L. D. Yao, J. Tikkanen, H. Huhtinen, R. Jha, V. P. S. Awana, S. van Dijken, and P. Paturi, J. Phys. Cond. Mat. **28**, 175702:1 (2016).

[22] H. Huhtinen, J. Ulriksson, M. Malmivirta, J. Järvinen, R. Jha, V. P. S. Awana, S. Vasiliev, and P. Paturi, IEEE T. Appl. Supercond. **27**, 7501205 (2017).

[23] M. M. Aye, M. Z. Khan, E. Rivasto, J. Tikkanen, H. Huhtinen, and P. Paturi, IEEE T. Appl. Supercond. **29**, 8000805 (2019).

[24] M. Peurla, H. Huhtinen, and P. Paturi, Supercond. Sci. Technol. **18**, 628 (2005).

[25] M. Peurla, P. Paturi, Y. P. Stepanov, H. Huhtinen, Y. Y. Tse, A. C. Bódi, J. Raittila, and R. Laiho, Supercond. Sci. Technol. **19**, 767 (2006).

[26] J. Ye and K. Nakamura, Phys. Rev. B **50**, 7099 (1994).

[27] H. P. Wiesinger, F. M. Sauerzopf, and H. W. Weber, Physica C **203**, 121 (1992).

[28] D. V. Shantsev, Y. M. Galperin, and T. H. Johansen, Phys. Rev. B **60**, 13112 (1999).

[29] A. Sanchez and C. Navau, Supercond. Sci. Technol. **7**, 444 (2001).

[30] A. V. Pan, I. A. Golovchansky, and S. A. Fedoseev, EPL **103**, 17006 (2013).

[31] A. B. Pippard, Physica **19**, 765 (1953).

[32] B. Stelzer, X. Chen, P. Bliem, M. Hans, B. Völker, R. Sahu, C. Scheu, D. Primetzhofer, and J. M. Schneider, Scientific reports **9**, 8266 (2019).

[33] E. Yoo, J. H. Moon, Y. S. Jeon, Y. Kim, J.-P. Ahn, and Y. K. Kim, Materials Characterization **166**, 110451 (2020).

[34] B. D. Cullity and S. R. Stock, *Elements of X-Ray Diffraction, 3rd ed.*, 1802 (Prentice Hall, 2001).

[35] O. Durand, A. Letoublon, D. Rogers, and F. H. Teherani, Thin Solid Films **519**, 6369 (2011).

[36] M. Chiao, R. W. Hill, C. Lupien, L. Taillefer, P. Lambert, R. Gagnon, and P. Fournier, Phys. Rev. B **62**, 3554 (2000).

[37] H. Palonen, H. Huhtinen, and P. Paturi, IEEE T. Appl. Supercond. **23**, 7200705 (2013).

[38] C. P. Poole Jr., H. A. Farach, R. J. Creswick, and R. Prozorov, *Superconductivity, Second Edition*, 1759 (Academic Press, 2007).

[39] E. H. Brandt, Phys. Rev. B **54**, 4246 (1996).

[40] T. Pereg-Barnea, P. J. Turner, R. Harris, G. K. Mullins, J. S. Bobowski, M. Raudsepp, R. Liang, D. A. Bonn, and W. N. Hardy, Phys. Rev. B **69**, 184513 (2004).

[41] P. Anderson, Journal of Physics and Chemistry of Solids **11**, 26 (1959).

[42] I. Bozovic, A. T. Bollinger, J. Wu, and X. He, Low Temperature Physics **44**, 519 (2018).

[43] I. Pallecchi, C. Tarantini, Y. Shen, R. K. Singh, N. Newman, P. Cheng, Y. Jia, H.-H. Wen, and M. Putti, Supercond. Sci. Technol. **31**, 034007 (2018).

[44] N. P. Shabanova, S. I. Krasnosvobodtsev, A. V. Varlashkin, and A. I. Golovashkin, Physics of the Solid State **44**, 1840 (2002).

[45] B. B. Goodman, J. Phys. Radium **23**, 704 (1962).

[46] F. C. Klaassen, G. Doornbos, J. M. Huijbregtse, R. C. F. van der Geest, B. Dam, and R. Griessen, Phys. Rev. B **64**, 184523 (2001).

[47] P. Paturi, M. Malmivirta, H. Palonen, and H. Huhtinen, IEEE T. Appl. Supercond. **26**, 8000705:1 (2016).

[48] D. Dew-Hughes, Philosophical magazine **30**, 293 (1974).

[49] D. Dew-Hughes, Supercond. Sci. Technol. **27**, 713 (2001).

[50] P. Paturi, M. Malmivirta, T. Hynninen, and H. Huhtinen, J. Phys. Cond. Mat. **30**, 315902:1 (2018).

[51] K. Haran, S. Kalsi, T. Arndt, H. Karmaker, R. Badcock, R. Buckley, T. Haugan, M. Izumi, D. Loder, J. Bray, P. Masson, and W. Stautner, Supercond. Sci. Technol. **30**, 123002 (2017).

[52] List of different values is available at http://hoffman.physics.harvard.edu/materials/ybco/

Acknowledgments